Magnetic and thermal characterization of Fe2.9wt.%Si for magnetic shielding applications

IEEE Access
Multidisciplinary | Rapid Review | Open Access Journal

Received 29 November 2024, accepted 23 December 2024, date of publication 30 December 2024,
date of current version 6 January 2025.

Digital Object Identifier 10.1109/ACCESS.2024.3524238

RESEARCH ARTICLE

Magnetic and Thermal Characterization of Fe2.9wt.%Si for Magnetic Shielding Applications

MICHELE QUERCIO[1], LUCA SANTORO[2], EMIR POSKOVIC[3], (Member, IEEE), RAFFAELLA SESANA[2], AND ALDO CANOVA[3], (Senior Member, IEEE)

[1]Department of Industrial, Electronic and Mechanical Engineering, University of Roma Tre, 00154 Rome, Italy
[2]Department of Mechanical and Aerospace Engineering, Politecnico di Torino, 10129 Turin, Italy
[3]Energy Department, Politecnico di Torino, 10129 Turin, Italy

Corresponding author: Michele Quercio (michele.quercio@uniroma3.it)

ABSTRACT This article provides an in-depth analysis of the magnetic shielding and thermal properties of additively manufactured materials, focusing on the Fe2.9wt.%Si alloy produced via Laser Powder Bed Fusion (LPBF). The study compares these materials' performance with conventional counterparts, particularly in the context of their application in magnetic shielding of a relay switch. The research integrates experimental findings from thermal imaging techniques to evaluate the efficiency of these materials under operational conditions, offering valuable insights into the future of additive manufacturing in high-performance magnetic shielding.

INDEX TERMS Active thermography, additive manufacturing, electromagnetic shielding.

I. INTRODUCTION

Additive Manufacturing (AM) technologies have become increasingly prominent in the industrial sector due to their ability to produce high-performing and complex components with intricate geometries and specific material properties [1], [2], [3], [4], [5], [6], [7], [8]. This flexibility has led to their widespread application in various industries, including aerospace [9], trends in manufacturing [10], and other industrial sectors [11]. Among the various AM techniques, Laser Powder Bed Fusion (LPBF) is particularly notable for its frequent use [12], [13]. The quality of components produced using AM is influenced by several factors, including process parameters such as laser power, scanning path, and scan speed, as well as the orientation of the component on the printing platform [14], [15]. Optimizing these parameters is crucial for minimizing defects, both on the surface and within the material. Common defects in AM components include impurities, keyhole collapse, solidification cracking, and surface-connected porosity [16]. While both destructive and non-destructive methods can be employed to detect these defects, non-destructive testing (NDT) is generally preferred due to the high production costs associated with AM [17]. NDT methods for defect detection can be categorized into in-line [18], [19], [20], [21] and post-production techniques [22], [23], [24]. Post-production methods include active infrared thermography (aIRT), X-ray computed tomography (CT), and ultrasonic testing (UT) [25]. Given that the powder materials used in AM undergo heat treatments that alter their physical and mechanical properties, it is essential to characterize the properties of the components after manufacturing. While previous studies have explored the effect of heat treatments on the electrical resistivity of AM materials [26], investigations into the magnetic properties of ferromagnetic materials across different processes and alloys have also been reported [27], [28], [29], [30], [31], [32], [33], [34]. In recent years, there has been significant interest in the measurement of thermal properties, particularly through active thermography techniques [35], [36]. Active thermography has been utilized for several decades as a non-destructive testing method [37], [38], [39], particularly for characterizing corrosion defects using halogen lamps as heat sources, as described in [40] and [41] introduced a laser-based active thermography approach coupled with a Digital Micromirror Device (DMD) array, which enables the identification of hidden defects and their dimensions. Tha authors in [42] conducted an analytical, numerical, and experimental study on the effects

The associate editor coordinating the review of this manuscript and approving it for publication was Guijun Li.

of thermal diffusivity and crack defects using flying spot laser thermography, a technique involving a moving laser heat source for linear scanning. In [43] and [44] laser stimulated thermography has been used for microstructural characterization through thermal diffusivity local measure. In fact, thermal diffusivity can be related to thermal and electrical conductivity or to mechanical properties such as hardness and so tensile strength. In [45], [46], [47], [48], and [49] laser stimulation is used to study the microstructural variation in the resistance spot weld. Further research by [50] examined defect characterization in anisotropic materials using active thermography with a halogen lamp, similar to the method described by [40]. Similarly, halogen lamps have been used for testing of anisotropic materials such as wooden materials [51]. In addition to halogen lamps, other excitation sources for active thermography include ultrasonic thermography [52], [53] and induction thermography [54], [55], [56], [57] evaluated the thermal diffusivity of boron steel specimens with different heat treatments using pulsed laser spot active thermography. Challenges in this methodology include the need for a precise setup to avoid heat losses and nonlinearities, as illustrated by [58], who used a vacuum jacket for thermal measurements. Subsequent studies applied this method to stripe-shaped samples [59] and for anisotropic thermal diffusivity measurements [60]. More advanced applications have explored the use of lock-in stimulation on transparent crystals [61] and semitransparent thin films [62]. The performance of magnetic shielding is influenced by factors such as permeability, electrical conductivity, thickness, and shape of the shield [34], [63], [64], [65], [66], [67], [68], [69]. Non-destructive evaluation of magnetic properties can enhance the design and verification of magnetic shielding, particularly when quality control is integrated with property control [70], [71], [72], [73], [74]. Despite the significance of this topic, there is limited literature on the assessment of electric and magnetic properties in AM-produced magnetic shields. Although some studies have been published on magnetic shields for high-frequency applications using polymeric materials [75], [76], [77], the area remains underexplored. In this work, the use of active thermography to analyze the thermal properties of a magnetic shield made of Fe2.9%Si was presented. The aim is to establish a rapid, reliable and non-destructive technique to measure and verify the shielding performance of magnetic shields and its thermal properties, especially for laboratory equipment that can be produced using AM. Furthermore, the present work aims to evaluate the magnetic shielding properties of ferromagnetic components produced by LPBF technique.

II. METHODOLOGY

The methodology for this study was designed to rigorously evaluate the magnetic shielding and thermal properties of the Fe2.9wt.%Si alloy produced via Laser Powder Bed Fusion (LPBF). The process was divided into several key stages: additive manufacturing process, magnetic performance evaluation and thermal analysis.

A. ADDITIVE MANUFACTURING PROCESS

The additive manufacturing of Fe2.9wt.%Si alloy was carried out using an industrial-scale LPBF system equipped with a multi-core fiber laser. The LPBF process involves spreading a thin layer of powder on a build platform, followed by the selective melting of the powder using a focused laser beam (see figure 1). The platform then lowers, and another layer of powder is spread, with the process repeating layer by layer until the part is complete. The printed sample is represented in figure 2. Key process parameters are reported in tab. 1, including laser power, scan speed, hatch spacing, and layer thickness, were optimized through preliminary experiments to achieve high-density samples with minimal porosity. The process parameters were fine-tuned to balance the energy input and ensure complete melting of the powder without causing excessive vaporization or defects such as keyholing or balling.

TABLE 1. A list of ideal process parameters utilized for creating highly dense samples.

Process parameters	Value
Laser power, P(W)	200
Scan speed, v(mm/s)	800
Hatch distance, $h_d(\mu m)$	70
Layer thickness, z(μm)	30
Hatching rotation, $\alpha(^\circ)$	67
Inert Gas type	Ar
Power emission mode	CW
Substrate material	AISI 316L

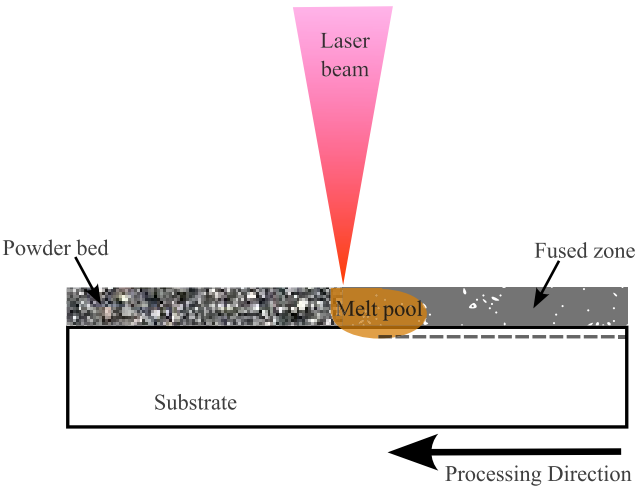

FIGURE 1. Layer-by-Layer manufacturing process (LPBF).

B. POST-PROCESSING AND HEAT TREATMENT

After the LPBF process, the samples were subjected to post-processing treatments to enhance their magnetic properties. Heat treatment consisted of annealing at 1200 °C for 1 h

under vacuum. This has allowed stress-relief to reduce residual stresses induced by the rapid cooling rates inherent to the LPBF process. The heat treatment was carefully controlled to avoid excessive grain growth while promoting the homogenization of the microstructure. Samples were characterized in both as-built and heat-treated conditions to assess the effects of post-processing on their properties.

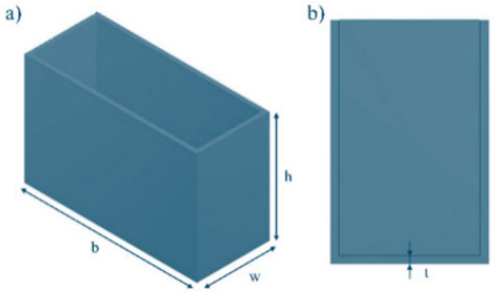

FIGURE 2. Geometry of the electromagnetic shield.

C. MAGNETIC AND ELECTROMAGNETIC PERFORMANCE EVALUATION

The magnetic properties of the Fe2.9wt.%Si alloy were evaluated through the standard toroidal test (see figure 3). Two toroidal samples were printed and used, one in As-Built (AB) condition and the other one after Heat Treatment (HT). The samples were subjected to hysteresis loop measurements to determine key magnetic properties such as permeability and coercitivity. The magnetic shielding factor (SF) of the samples was measured using a structure made by Fused Deposition Modeling (FDM)(the red one in figure 4). This type of measurement involves placing the sample (named AM shield in figure 4.a) inside this structure and using a coil or a permanent magnet to measure the attenuation of electromagnetic waves in frequency or stationary condition (see figure 4). As reported in figure 4.b, three different measuring points were designed at different heights and positions in order to analyze the shielding properties of the printed samples. A PLA support structure (the white one in figure 4.a) was created using the FDM technique to insert the field probe to evaluate the attenuation of the magnetic field at different positions inside the magnetic shield. Both experimental setups and numerical simulations were employed to assess the SF, with simulations used to model the effects of different geometries and material compositions.

D. THERMAL PROPERTIES ANALYSIS

In this work, we used laser-stimulated active thermography to assess the thermal properties of our specimens. A FLIR A6751sc infrared thermal camera with a sensitivity of less than 20 mK was employed, as shown in Figure 5;The integration of the components has the commercial name Multi-DES. The laser source provided up to 50 W of power,

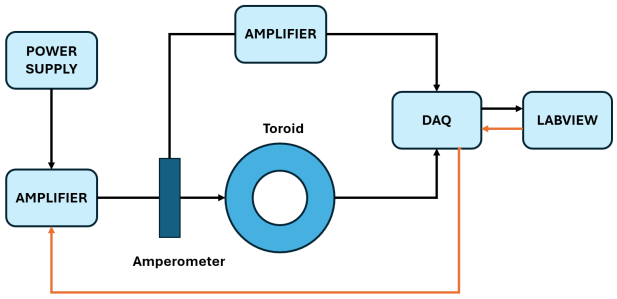

FIGURE 3. Toroidal test setup.

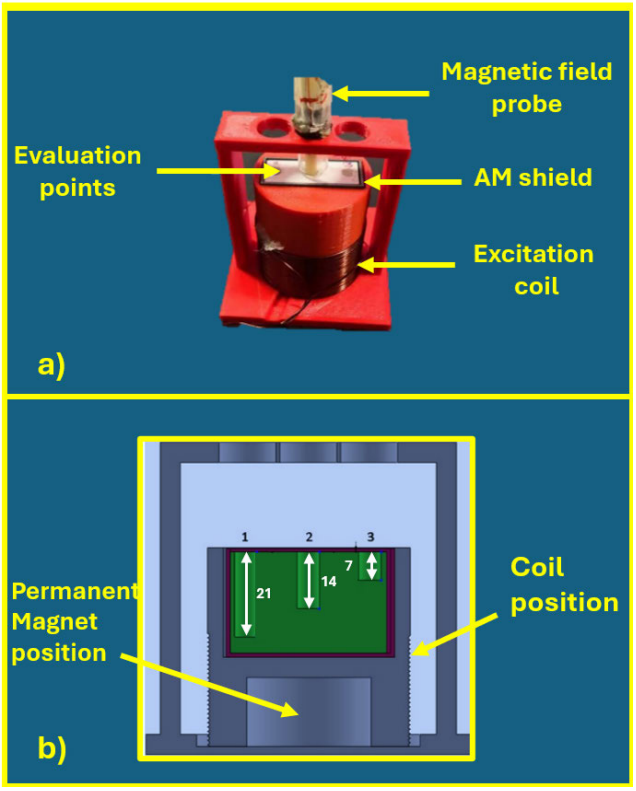

FIGURE 4. Magnetic field measurement test setup. a) structure realized by fused deposition modeling (FDM) technique; b) CAD identifying the evaluation points.

focused into a 2 mm diameter circular spot and controlled via a PC interface, as illustrated in Figure 6. The system was operated in reflection mode to ensure high spatial calibration accuracy.

A Lock-In laser thermography technique was utilized by applying 25 step pulses modulated at 1 Hz. All experiments were conducted under controlled environmental conditions (26 °C, 30% RH) with a 530 mm distance between the IR camera and the specimen. The parameters for the field of view (FOV), including the horizontal field of view (HFOV), vertical field of view (VFOV), and instantaneous field of view (IFOV), are summarized in Table 2.

To avoid any non-linear thermal responses, both laser power and frame rate were carefully monitored and

TABLE 2. Field of view (FOV) parameters.

HFOV	VFOV	IFOV
200 mm	160 mm	0.32 mm

controlled. Statistical validation methods were employed to ensure reliability and repeatability of the measurements.

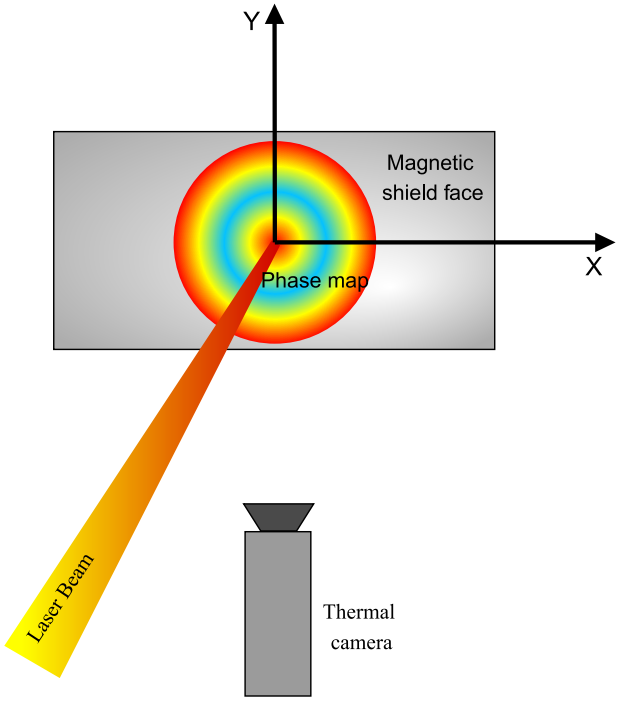

FIGURE 5. Active thermography setup. The laser source is directed onto the specimen, and the IR camera is positioned to capture the induced thermal response.

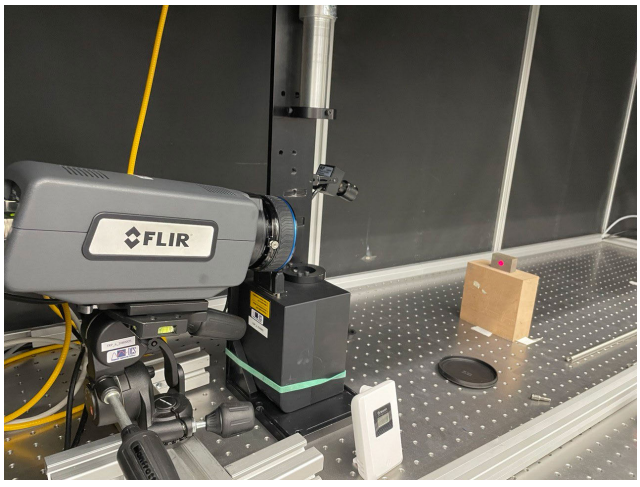

FIGURE 6. Laboratory setup of the active thermography. Laser and camera are aligned in reflection mode to maximize spatial resolution.

A dedicated Python routine was developed to perform phase analysis using a Lock-In Amplifier algorithm. This approach calculates the phase and amplitude of the thermal signal at the lock-in frequency more efficiently than a conventional fast Fourier transform (FFT). As a result, the phase plots generally exhibited symmetric and linear trends away from the heat source.

1) RELATIONSHIP BETWEEN PHASE SLOPE AND THERMAL DIFFUSIVITY

Following the methodology in [78], the slope m of the linear portion of the phase plot correlates to the thermal diffusivity D_x and the Lock-In test frequency f. This relationship can be expressed as:

$$m = -\sqrt{\frac{\pi f}{D_x}}. \tag{1}$$

Here, m does not provide an exact point-by-point analytical comparison but rather highlights how the intrinsic heat propagation speed (captured by D_x) affects the slope of the phase decay.

2) DEFINITION OF THERMAL DIFFUSIVITY

Thermal diffusivity D_x represents how quickly heat spreads through a material:

$$D_x = \frac{k}{\rho\, c}, \tag{2}$$

where k is thermal conductivity, ρ is density, and c is specific heat capacity. Although *Eq.* (2) does not yield a site-specific solution for non-homogeneous or anisotropic materials, it guides the interpretation of how fundamental material properties collectively govern heat flow.

3) ESTIMATION OF THE SLOPE AND THERMAL DIFFUSION LENGTH

To mitigate noise at larger distances from the laser spot, data points with amplitudes below 0.3 K are excluded. A linear polynomial is fitted to the remaining data, yielding the slope m. We further relate m to the thermal diffusion length μ, which describes the radial distance at which the phase decreases by 1 radian from the center of the heat source:

$$m = \frac{1}{\mu}. \tag{3}$$

If an *expected* value for μ, denoted $\mu_{expected}$, is available, it can be associated with a predicted diffusivity $D_{expected}$ by:

$$\mu_{expected} = \sqrt{\frac{D_{expected}}{\pi f}}. \tag{4}$$

4) PROCEDURE FOR DEFINING THE FITTING DOMAIN

To determine the radial domain where the slope remains linear, we use the estimated thermal diffusion length $\mu_{expected}$. The total radial extent r_{ext} for curve fitting is:

$$r_{ext} = 2\, r_{\text{laser spot}} + 2\, \mu_{expected}. \tag{5}$$

Thus, the fitting domain is:

$$[\,0 + 2\,r_{\text{laser spot}},\ 0 + 2\,r_{\text{laser spot}} + 2\,\mu_{expected}\,]. \quad (6)$$

This approach avoids distortions near the beam center and excessive noise at larger radii.

5) AUTOMATED RADIAL ANALYSIS AND FINAL OUTPUT

An automated routine finds the centroid of the laser spot and iteratively fits the linear region of the phase plot, yielding a best-fit diffusivity D_{fit}. Because specimens in this study may exhibit anisotropy, the calculation is repeated at multiple angular positions (from 0 to 360 degrees). The final reported diffusivity is thus an average that takes directional variations into account.

6) RELEVANCE AND CONTEXT FOR EXPERIMENTAL COMPARISON

Although the above equations describe the core physics of heat propagation and guide the phase-plot analysis, they do not yield an exact analytical solution for each measured radial point. Instead, they offer a framework to interpret and compare local thermal diffusivities in materials that could be non-homogeneous (e.g., additively manufactured specimens). By introducing a controlled, frequency-modulated heat wave (Lock-In thermography) and studying the resulting phase shift, we obtain consistent diffusivity estimates and can compare how heat flow varies at different locations in the same component.

7) SUMMARY OF EXPERIMENTAL PROCEDURE

In brief, a frequency-modulated (1 Hz) laser beam introduced a heat wave onto the specimen. Lock-In active thermography measurements were subsequently analyzed using phase-slope fitting and thermal diffusion length definitions to yield quantitative values for D_x in multiple directions (e.g., x, y, and in-between angles). This technique is especially well-suited for studying small or anisotropic components without relying on closed-form solutions for each test.

E. DATA ANALYSIS AND CORRELATION

The experimental data collected from the microstructural, magnetic, and thermal analyses were systematically correlated to understand the relationships between the LPBF process parameters, material microstructure, and overall performance. Statistical analysis was conducted to identify significant trends and to quantify the impact of different variables on the material's shielding effectiveness and thermal management capabilities.

III. RESULTS AND DISCUSSION

A. MAGNETIC AND ELECTROMAGNETIC SHIELDING PERFORMANCE

The Fe2.9wt.%Si alloy, produced via LPBF, exhibits highly promising magnetic shielding properties that have been meticulously analyzed in both its as-built and heat-treated

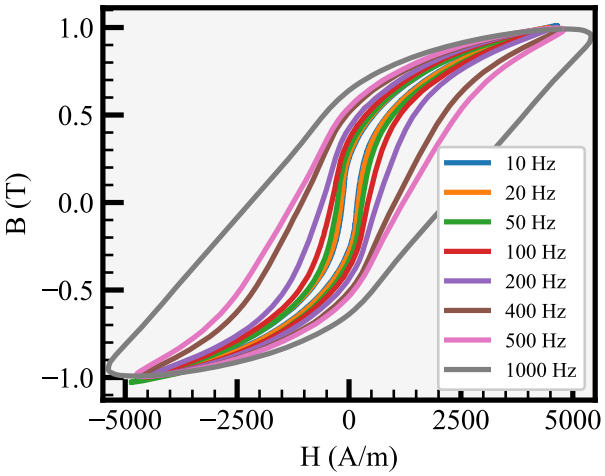

(a) Hysteresis loop of Fe2.9wt.%Si without heat treatment

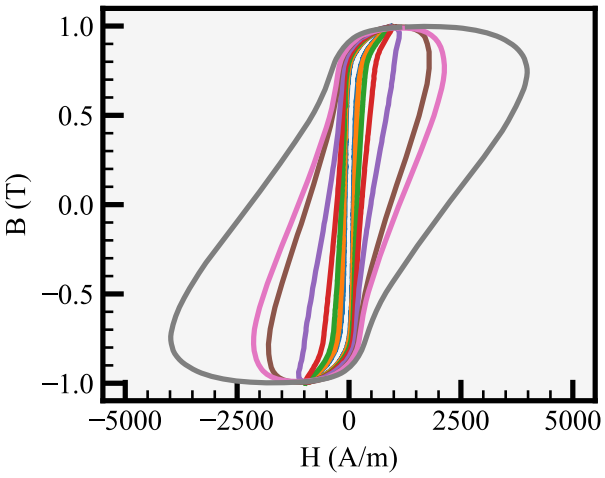

(b) Hysteresis loop of Fe2.9wt.%Si with heat treatment

FIGURE 7. Hysteresis loops of Fe2.9wt.%Si alloy at different frequencies and conditions.

conditions. figure 7 and 8 present detailed analyses of the hysteresis loops and magnetic permeability of the Fe2.9wt.%Si alloy under various conditions. The hysteresis loop data, shown in Figure 7, provides critical insight into the magnetic behavior of the material, illustrating how the magnetic induction (B) varies with the applied magnetic field strength (H) at different frequencies. Notably, the hysteresis loops for the as-built sample (figure 7.a) demonstrate a wider loop area compared to the heat-treated sample (figure 7.b), indicating higher energy losses due to magnetic hysteresis in the as-built condition. This difference suggests that the heat treatment process effectively reduces the coercivity of the material, leading to improved magnetic properties such as lower hysteresis losses and enhanced soft magnetic behavior. On the other hand, the enlargement of the loops at high frequencies is due to the increment of eddy currents, which has a higher effect after the heat

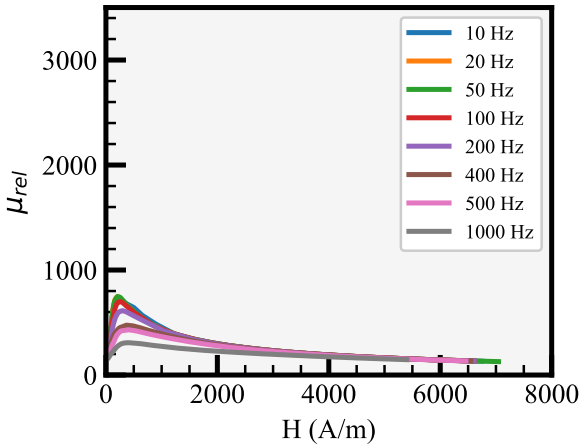

(a) Magnetic permeability of Fe2.9wt.%Si without heat treatment

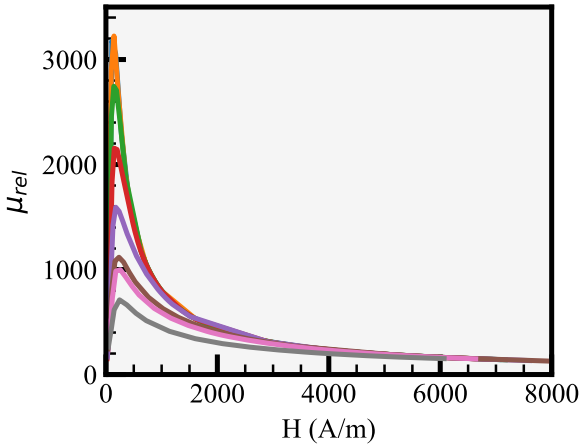

(b) Magnetic permeability of Fe2.9wt.%Si with heat treatment

FIGURE 8. Magnetic permeability trends of Fe2.9wt.%Si alloy under different conditions.

treatment. The magnetic permeability trends, illustrated in figure 8, further underscore the impact of heat treatment on the material's magnetic performance. In the as-built condition (figure 8.a), the relative magnetic permeability (μ_{rel}) peaks at lower values compared to the heat-treated condition (figure 8b). This enhancement in magnetic permeability post-heat treatment suggests that the material undergoes significant microstructural changes, such as grain growth and stress relief, which facilitate more efficient magnetic domain movement. As a result, the heat-treated Fe2.9wt.%Si alloy demonstrates superior performance in applications requiring high magnetic permeability, making it an excellent candidate for magnetic shielding in sensitive electronic environments. The effectiveness of the Fe2.9wt.%Si alloy as a magnetic shield is quantitatively represented by the Shielding Factor (SF) described as:

$$SF = \frac{|B_0(x, y, z)|}{|B_S(x, y, z)|} \tag{7}$$

where:

- B_0 is the magnetic induction at a certain point when the shield is absent.
- B_S is the magnetic induction at a certain point when the shield is applied.

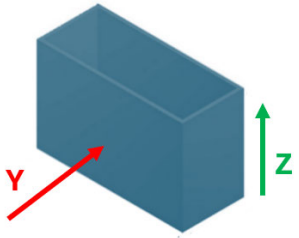

FIGURE 9. Electromagnetic field excitation directions.

This characteristic measures the material's ability to attenuate electromagnetic fields. Figures 10 and 11 provide a comprehensive overview of the SF under both DC and AC/DC excitation conditions. The data presented in Figure 10 shows the SF at different evaluation points along the Z and Y directions of the shield (see figure 9), highlighting the superior performance of the heat-treated samples over the as-built ones in DC condition, particularly at the critical evaluation points where maximum electromagnetic exposure occurs. This trend is consistent across both directional analyses, reinforcing the conclusion that heat treatment enhances the shielding effectiveness by refining the microstructure, reducing defects, and homogenizing the material properties. Further analysis of the SF under AC/DC excitation, depicted in Figure 11, reveals the material's frequency-dependent shielding performance. The comparison between simulated and experimentally measured SF values across different evaluation points provides valuable insights into the material's behavior under varying electromagnetic conditions. The data shows that the heat-treated Fe2.9wt.%Si alloy consistently outperforms the as-built alloy, particularly in the higher frequency range (kHz), where electromagnetic interference (EMI) is most challenging to mitigate. The relative error heatmaps in Figure 12 provide a visual representation of the discrepancies between the simulated and experimental SF data. These heatmaps highlight the accuracy of the simulations in predicting the magnetic shielding behavior of the Fe2.9wt.%Si alloy, with minimal relative errors observed across most frequency ranges and evaluation points. The slight variations seen in certain areas underscore the complex interplay between the material's microstructure and its magnetic properties, which could be further refined through additional process optimization and detailed modeling. Overall, the analysis presented here demonstrates that the Fe2.9wt.%Si alloy, particularly after heat treatment, offers excellent magnetic shielding performance, with potential applications in a variety of frequency applications and sensitive environments. The LPBF process's ability to produce complex geometries further enhances this

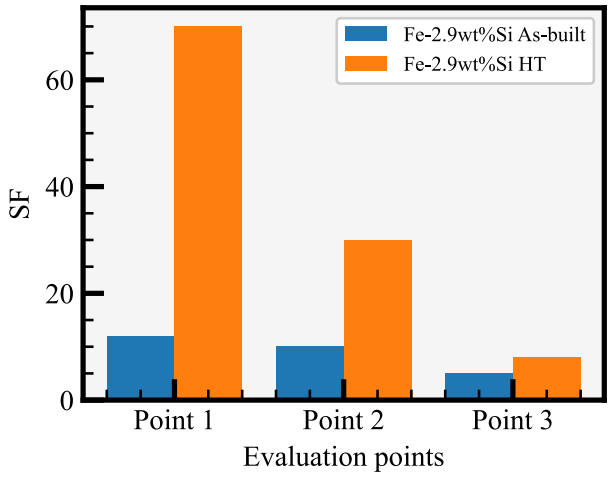

(a) Direction Z

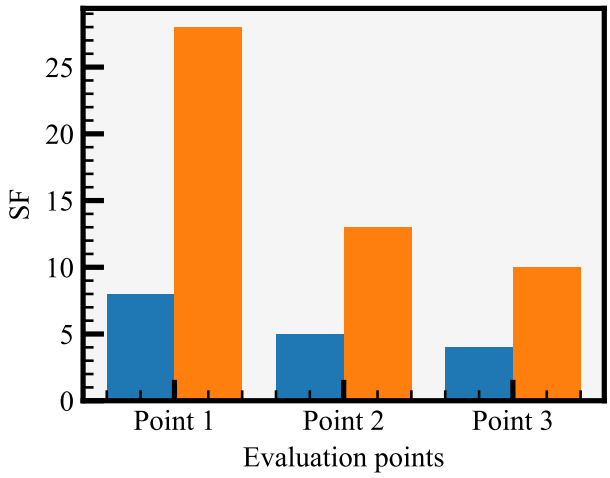

(b) Direction Y

FIGURE 10. Shielding Factor of Fe2.9wt.%Si alloy electromagnetic shield with DC excitation at different evaluation points.

material's utility, providing a versatile and effective solution for modern electromagnetic interference challenges.

B. MICROSTRUCTURAL ANALYSIS

The two shields, in their as-built (AB) and heat-treated (HT) conditions, were polished on the X-Y deposition plane to prepare them for detailed microstructural analysis. Optical microscopy was employed to capture high-resolution images of the specimens, which allowed for the evaluation of pore presence, geometry, and distribution within the material. A comparative analysis of the microstructures in different conditions is shown in figure 13, which highlights the differences between the as-built and heat-treated specimens.

In figure 13, microstructural features are presented under different conditions: figure 13.a shows the as-built (AB) specimen after chemical etching. This image reveals the grain structure and distribution of phases within the material. The grain boundaries are distinctly visible, indicating a relatively coarse microstructure typical of the as-built condition, where rapid solidification has led to the formation of large grains with minimal refinement. The etching process accentuates these features, providing a clearer view of the internal structure. figure 13.b illustrates the unetched as-built (AB) specimen. Without etching, the image primarily shows the distribution of pores and other discontinuities within the material. The pores appear as dark, irregularly shaped regions scattered throughout the matrix. These are typical of the as-built condition, where the rapid solidification process can trap gas or lead to incomplete fusion, resulting in porosity. figure 13.c presents the heat-treated (HT) specimen in an unetched state. Here, a noticeable reduction in the number and size of pores can be observed, compared to the as-built condition. Heat treatment has contributed to the healing of some of the pores through mechanisms such as diffusion and recrystallization, leading to a more homogenous and refined microstructure. The absence of etching in this image means the focus is primarily on the reduction of porosity rather than the detailed grain structure. The chemical etching applied to the as-built specimen in figure 13.a provides insight into the material's inherent microstructure, revealing the presence of larger grains and potential columnar structures that have formed during the additive manufacturing process. In contrast, the heat-treated specimen, although not etched, demonstrates a more uniform distribution of smaller grains, suggesting that the heat treatment has been effective in reducing internal stresses and homogenizing the microstructure. Overall, the comparison of these images demonstrates that heat treatment significantly alters the microstructure by refining the grain size and reducing porosity as demonstrated by the same authors in [66], where it is also possible to find the microstructure image and the value of the grain size before and after heat treatment. These changes are consistent with observations in the literature, where heat treatment is known to enhance the magnetic properties of additively manufactured materials by reducing defects and promoting a more stable and uniform microstructure [79], [80], [81].

C. THERMAL PERFORMANCE

The thermal performance of the Fe2.9wt.%Si alloy was evaluated to understand the impact of heat treatment on its thermal properties, particularly thermal diffusivity. Lock-in thermography was employed as a non-destructive technique to measure the thermal response of the material under cyclic heating. This method provides insights into the thermal diffusivity by analyzing the phase and amplitude of thermal waves as they propagate through the material. figure 14 presents the results from the lock-in thermography tests conducted on the as-built specimen. The amplitude and phase maps in figure 14 allow for the visualization of the thermal wave propagation within the material. The unprocessed amplitude map shows a relatively uniform distribution, which

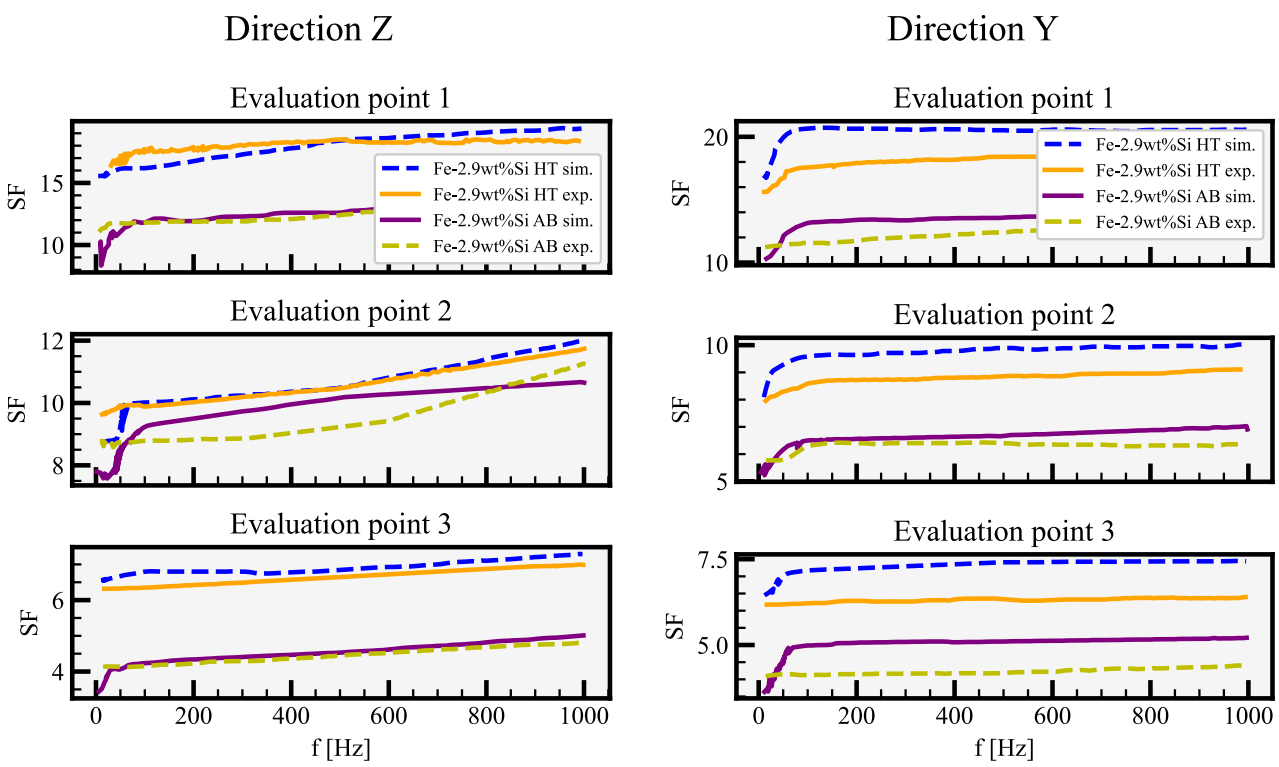

(a) Comparison of SF values between simulated and experimentally measured data along the axial direction for the three different measurement points, using AC/DC excitation.

(b) Comparison of SF values between simulated and experimentally measured data along the transverse direction for the three different measurement points, using AC/DC excitation.

FIGURE 11. Comparison of Shielding Factor (SF) values between simulated and experimentally measured data for Fe2.9wt.%Si alloy under AC/DC excitation conditions.

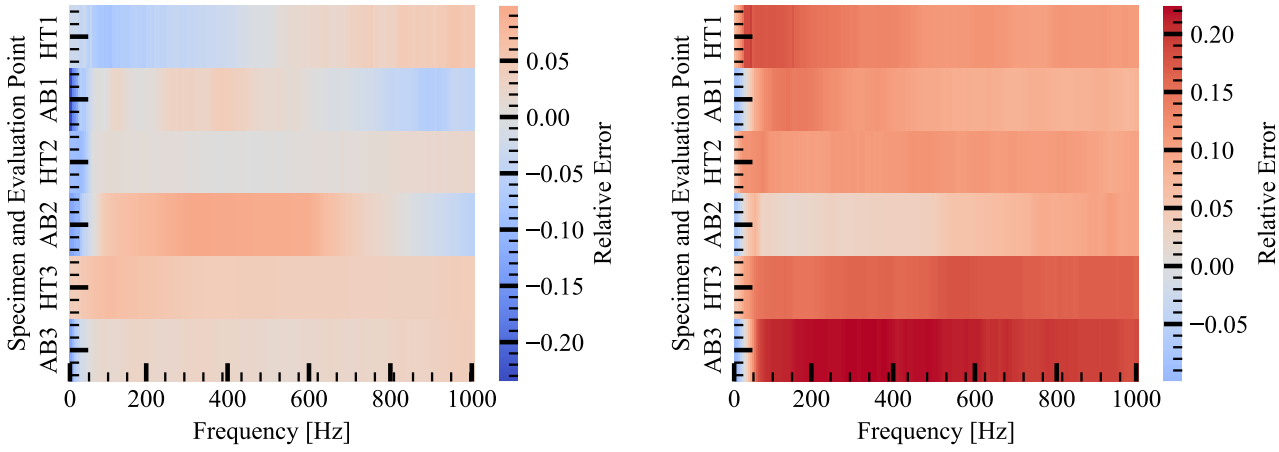

(a) Relative error between simulated and experimental SF values in Direction Z.

(b) Relative error between simulated and experimental SF values in Direction Y.

FIGURE 12. Relative error heatmaps for SF values of Fe2.9wt.%Si alloy across different frequencies and evaluation points.

corresponds to the material's inherent thermal response. In contrast, the phase map reveals more detailed information about the material's internal structure, highlighting regions where the phase shift occurs due to variations in thermal properties. Further processing of the lock-in thermography data, as shown in the lower half of figure 14, involves

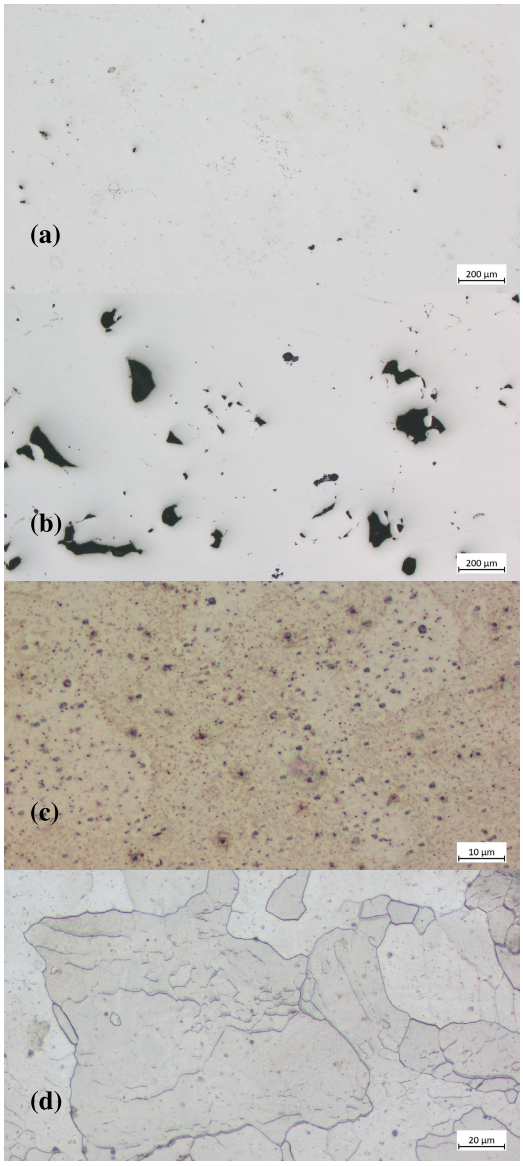

FIGURE 13. Microstructural comparison: a) HT unetched, b) AB unetched, c) HT etched, d) AB etched.

the creation of masked amplitude and phase maps. These processed maps focus on specific areas of interest within the material, excluding noise and irrelevant regions. The masked amplitude map emphasizes the thermal diffusivity in selected areas, while the masked phase map sharpens the focus on phase shifts that indicate thermal inhomogeneities or voids within the structure. The comparison between the raw and processed data reveals that the heat treatment likely contributes to a more uniform thermal response, reducing phase lag and improving overall thermal diffusivity. The impact of heat treatment on thermal diffusivity is further elucidated in figure 15, which compares the diffusivity values as a function of directional angle for both the as-built and heat-treated samples. The data, obtained using a Python algorithm, illustrates that the heat-treated sample exhibits

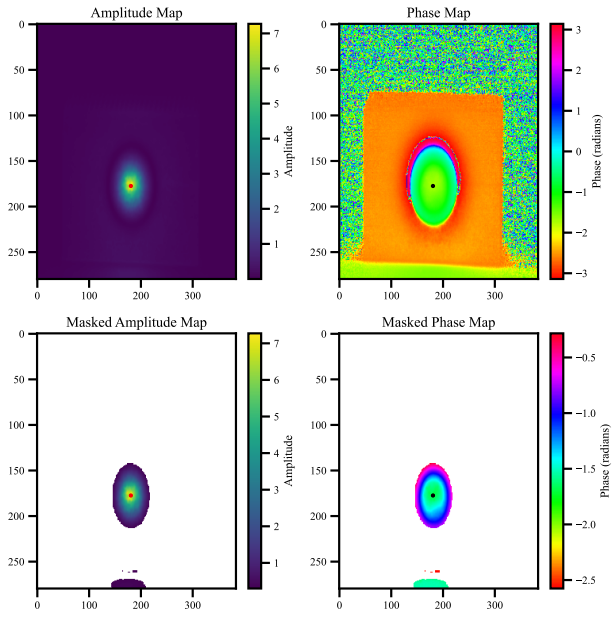

FIGURE 14. Amplitude map (left) and Phase Map (right), respectevely the full data (top) and masked data in the interest area (bottom).

consistently higher diffusivity values across all directional angles compared to the as-built sample. This uniform increase in diffusivity is indicative of the microstructural improvements achieved through heat treatment, such as reduced porosity and grain refinement, which enhance the material's ability to conduct heat more efficiently.

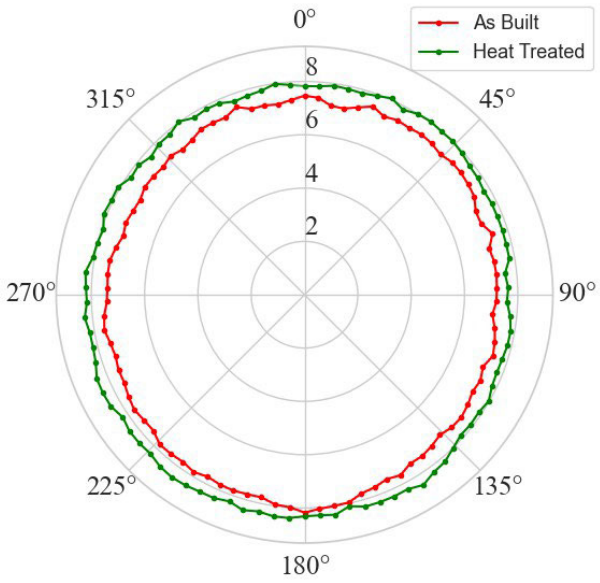

FIGURE 15. Diffusivity values versus direction angle for as-built (red dots) and heat-treated (green dots) samples.

Tab. 3 summarizes the average directional diffusivity values for the two specimens, averaged over 360 degrees. The results clearly demonstrate that the heat-treated specimens

possess higher average diffusivity values compared to their as-built counterparts. The standard deviation is also slightly lower in the heat-treated samples, suggesting a more consistent thermal performance across different directions.

TABLE 3. Average experimental directional diffusivity over 360 degrees.

	$D_x[\text{mm}^2/\text{s}]$	$StandardDeviation[\text{mm}^2/\text{s}]$
As-Built	7.527	0.0107
Heat Treated	8.044	0.0091

The observed improvement in thermal diffusivity due to heat treatment can be attributed to several factors. First, the heat treatment process likely reduces the number and size of voids within the material, as evidenced by the less steep slope observed in the phase map of the heat-treated specimen. This reduction in voids leads to a denser microstructure, which enhances the material's ability to conduct heat. The correlation between the phase plot's slope and the material's thermal properties underscores the importance of microstructural uniformity in achieving superior thermal performance. Furthermore, the literature supports the notion that heat treatment can enhance thermal conductivity by promoting microstructural changes such as grain growth and the reduction of residual stresses [82]. These changes result in a more homogenous and stable structure, which is better suited for efficient heat conduction. In the case of the Fe2.9wt.%Si alloy, the combination of reduced void content and optimized grain structure likely contributes to the observed increase in thermal diffusivity across all directions. Overall, the study highlights the significant impact of heat treatment on the thermal properties of additively manufactured Fe2.9wt.%Si alloy samples. By enhancing the material's thermal diffusivity, heat treatment improves the overall thermal performance, making the alloy more suitable for applications where efficient heat dissipation is critical. The consistent superiority of the heat-treated samples across all measured parameters reinforces the value of thermal treatment in optimizing the performance of additively manufactured materials.

IV. CONCLUSION

This study examined the thermal and magnetic properties of a Fe2.9%Si alloy fabricated via Laser Powder Bed Fusion (LPBF) in both as-built and heat-treated conditions. The findings highlight the significant impact of heat treatment on enhancing material performance. Heat treatment notably improved the alloy's magnetic properties, resulting in reduced coercivity and hysteresis losses, which indicate better soft magnetic behavior. Additionally, there was an increase in magnetic permeability due to enhanced microstructural refinement, leading to an improved magnetic shield factor (SF) that makes the alloy suitable for low-frequency magnetic field applications. In terms of thermal properties, heat-treated samples exhibited a marked increase in thermal diffusivity, enhancing their ability to conduct heat. The thermal diffusivity became more uniform across directional angles after treatment, ensuring consistent thermal management. Furthermore, microstructural densification reduced porosity, facilitating more efficient heat conduction. As illustrated in Figure 16, heat-treated samples outperform their as-built counterparts in both thermal and magnetic domains. Overall, these results underscore the critical role of heat treatment in optimizing material properties for advanced applications.

Implications and Future Applications:

- **Versatile Industrial Applications:** The enhanced magnetic and thermal properties make the heat-treated Fe2.9%Si alloy suitable for a wide range of applications, including aerospace and electronics.
- **Customization Potential:** The combination of LPBF and precise heat treatment protocols allows for tailored material properties to meet specific operational requirements.
- **Future Research Directions:** Further optimization of heat treatment parameters and exploration of the alloy's performance in specific application environments are recommended to fully leverage its potential.

Overall, the heat-treated Fe2.9%Si alloy exhibits enhanced magnetic and thermal properties, positioning it as a promising candidate for applications requiring superior magnetic shielding and effective thermal management. The ability to fine-tune these properties through controlled fabrication and post-processing techniques highlights the alloy's versatility and potential for broad industrial adoption.

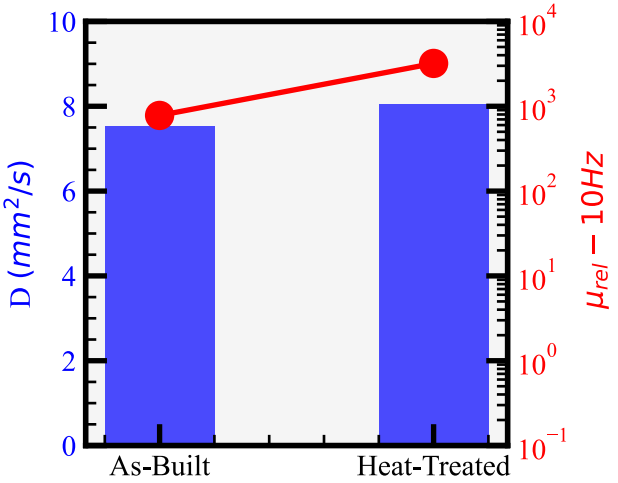

FIGURE 16. Comparisons of thermal VS magnetic properties.

ACKNOWLEDGMENT

The research group of Prof. Barbara Previtali of Politecnico di Milano for the realization of the components produced by additive manufacturing technology.

REFERENCES

[1] S. A. M. Tofail, E. P. Koumoulos, A. Bandyopadhyay, S. Bose, L. O'Donoghue, and C. A. Charitidis, "Additive manufacturing: Scientific and technological challenges, market uptake and opportunities," *Mater. Today*, vol. 21, no. 1, pp. 22–37, Jul. 2017. [Online]. Available: https://www.sciencedirect.com/science/article/pii/S1369702117301773

[2] H. Wang, F. Wen, D. Liu, G. Zhang, Y. Liu, J. Wang, and L. Zou, "Iron-based soft magnetic materials fabricated by laser additive manufacturing," *Engineered Sci.*, vol. 22, p. 809, Jan. 2023.

[3] I. Galarreta-Rodriguez, A. López-Ortega, E. Garayo, J. J. Beato-López, P. L. Roca, V. Sánchez-Alarcos, V. Recarte, C. Gómez-Polo, and J. I. Pérez-Landazábal, "Magnetically activated 3D printable polylactic acid/polycaprolactone/magnetite composites for magnetic induction heating generation," *Adv. Compos. Hybrid Mater.*, vol. 6, no. 3, p. 102, May 2023.

[4] S. Jambhulkar, D. Ravichandran, V. Thippanna, D. Patil, and K. Song, "A multimaterial 3D printing-assisted micropatterning for heat dissipation applications," *Adv. Comp. Hybrid Mater.*, vol. 6, no. 3, pp. 1–16, May 2023.

[5] X. Wang, Z. Liu, H. Wang, and C. Zeng, "Direct 3D printing of piezoelectrets: Process feasibility, prototypes fabrication and device performance," *Engineered Sci.*, vol. 21, p. 800, Jan. 2022.

[6] A. Manoj and R. C. Panda, "Biodegradable filament for 3D printing process: A review," *Engineered Sci.*, vol. 18, pp. 11–19, Jan. 2022.

[7] X. Wang, Z. Liu, H. Wang, and C. Zeng, "An electro-mechanical coupled model for 3D printed piezoelectrets: Development, validation, and prediction," *Engineered Sci.*, vol. 24, p. 899, Jan. 2023.

[8] X. Zhang, M. Dong, X. Cai, D. Chen, Y. Xian, X. Zheng, Z. Guo, and H. Algadi, "Progress in machining-induced residual stress and microstructural evolution of inhomogeneous materials and composites," *Adv. Compos. Hybrid Mater.*, vol. 6, no. 3, p. 122, Jun. 2023.

[9] A. Uriondo, M. Esperon-Miguez, and S. Perinpanayagam, "The present and future of additive manufacturing in the aerospace sector: A review of important aspects," *Proc. Inst. Mech. Eng., G, J. Aerosp. Eng.*, vol. 229, no. 11, pp. 2132–2147, Sep. 2015, doi: 10.1177/0954410014568797.

[10] C. Beyer, "Strategic implications of current trends in additive manufacturing," *J. Manuf. Sci. Eng.*, vol. 136, no. 6, Dec. 2014, Art. no. 064701, doi: 10.1115/1.4028599.

[11] E. Rauch, M. Unterhofer, and P. Dallasega, "Industry sector analysis for the application of additive manufacturing in smart and distributed manufacturing systems," *Manuf. Lett.*, vol. 15, pp. 126–131, Dec. 2017. [Online]. Available: https://www.sciencedirect.com/science/article/pii/S2213846317300925

[12] S. A. Kumar, A. S. Reddy, S. Mathias, A. Shrivastava, and R. V. S. Prasad, "Influence of post-processing techniques on the microstructure, properties and surface integrity of al Si mg alloy processed by laser powder bed fusion technique," *Surf. coatings Technol.*, vol. 425, Sep. 2021, Art. no. 127679.

[13] A. Raja, S. Rakesh, P. Gupta, N. J. Vasa, and R. Jayaganthan, "A review on the fatigue behaviour of AlSi10Mg alloy fabricated using laser powder bed fusion technique," *J. Mater. Res. Technol.*, vol. 17, pp. 1013–1029, Jan. 2022.

[14] M. Garibaldi, I. Ashcroft, N. Hillier, S. A. C. Harmon, and R. Hague, "Relationship between laser energy input, microstructures and magnetic properties of selective laser melted fe-6.9%wt Si soft magnets," *Mater. Characterization*, vol. 143, pp. 144–151, Sep. 2018.

[15] H. Choo, K.-L. Sham, J. Bohling, A. Ngo, X. Xiao, Y. Ren, P. J. Depond, M. J. Matthews, and E. Garlea, "Effect of laser power on defect, texture, and microstructure of a laser powder bed fusion processed 316L stainless steel," *Mater. Des.*, vol. 164, Dec. 2018, Art. no. 107534.

[16] M. C. Brennan, J. S. Keist, and T. A. Palmer, "Defects in metal additive manufacturing processes," *J. Mater. Eng. Perform.*, vol. 30, no. 7, pp. 4808–4818, Jul. 2021, doi: 10.1007/s11665-021-05919-6.

[17] P. Charalampous, I. Kostavelis, and D. Tzovaras, "Non-destructive quality control methods in additive manufacturing: A survey," *Rapid Prototyping J.*, vol. 26, no. 4, pp. 777–790, Mar. 2020, doi: 10.1108/rpj-08-2019-0224.

[18] S. Everton, M. Hirsch, P. Stravroulakis, R. Leach, and A. T. Clare, "Review of in-situ process monitoring and in-situ metrology for metal additive manufacturing," *Mater. Des.*, vol. 95, pp. 431–445, Jan. 2016. [Online]. Available: https://www.sciencedirect.com/science/article/pii/S0264127516300995

[19] B. Zhang, S. Liu, and Y. C. Shin, "In-process monitoring of porosity during laser additive manufacturing process," *Additive Manuf.*, vol. 28, pp. 497–505, May 2019. [Online]. Available: https://www.sciencedirect.com/science/article/pii/S2214860419303653

[20] G. Tapia and A. Elwany, "A review on process monitoring and control in metal-based additive manufacturing," *J. Manuf. Sci. Eng.*, vol. 136, no. 6, Dec. 2014, Art. no. 060801, doi: 10.1115/1.4028540.

[21] L. Santoro, R. Sesana, R. M. Nardo, and F. Curá, "Infrared in-line monitoring of flaws in steel welded joints: A preliminary approach with SMAW and GMAW processes," *Int. J. Adv. Manuf. Technol.*, vol. 128, nos. 5–6, pp. 2655–2670, Aug. 2023.

[22] M. S. Carvalho, A. P. Martins, and T. G. Santos, "Simulation and validation of thermography inspection for components produced by additive manufacturing," *Appl. Thermal Eng.*, vol. 159, May 2019, Art. no. 113872. [Online]. Available: https://www.sciencedirect.com/science/article/pii/S1359431119308506

[23] S. Senck, M. Happl, M. Reiter, M. Scheerer, M. Kendel, J. Glinz, and J. Kastner, "Additive manufacturing and non-destructive testing of topology-optimised aluminium components," *Nondestruct. Test. Eval.*, vol. 35, no. 3, pp. 315–327, Jul. 2020, doi: 10.1080/10589759.2020.1774582.

[24] Q. Y. Lu and C. H. Wong, "Applications of non-destructive testing techniques for post-process control of additively manufactured parts," *Virtual Phys. Prototyping*, vol. 12, no. 4, pp. 301–321, Oct. 2017, doi: 10.1080/17452759.2017.1357319.

[25] C. G. Kolb, K. Zier, J.-C. Grager, A. Bachmann, T. Neuwirth, S. Schmid, M. Haag, M. Axtner, F. Bayerlein, C. U. Grosse, and M. F. Zaeh, "An investigation on the suitability of modern nondestructive testing methods for the inspection of specimens manufactured by laser powder bed fusion," *Social Netw. Appl. Sci.*, vol. 3, no. 7, p. 713, Jun. 2021, doi: 10.1007/s42452-021-04685-3.

[26] C. Silbernagel, I. Ashcroft, P. Dickens, and M. Galea, "Electrical resistivity of additively manufactured AlSi10Mg for use in electric motors," *Additive Manuf.*, vol. 21, pp. 395–403, Mar. 2018. [Online]. Available: https://www.sciencedirect.com/science/article/pii/S2214860418300769

[27] M. Garibaldi, I. Ashcroft, J. N. Lemke, M. Simonelli, and R. Hague, "Effect of annealing on the microstructure and magnetic properties of soft magnetic fe-Si produced via laser additive manufacturing," *Scripta Mater.*, vol. 142, pp. 121–125, Aug. 2017. [Online]. Available: https://www.sciencedirect.com/science/article/pii/S1359646217305067

[28] C. Wang, X. Liu, T. Yang, D. Sridhar, H. Algadi, B. B. Xu, Z. M. El-Bahy, H. Li, Y. Ma, T. Li, and Z. Guo, "An overview of metal-organic frameworks and their magnetic composites for the removal of pollutants," *Separat. Purification Technol.*, vol. 320, May 2023, Art. no. 124144.

[29] J. Zeng, W. Xie, Y. Guo, T. Zhao, H. Zhou, Q. Wang, H. Li, Z. Guo, B. B. Xu, and H. Gu, "Magnetic field facilitated electrocatalytic degradation of tetracycline in wastewater by magnetic porous carbonized phthalonitrile resin," *Appl. Catal. B, Environ.*, vol. 340, Aug. 2023, Art. no. 123225.

[30] H. Cheng, L. Xing, Y. Zuo, Y. Pan, M. Huang, A. Alhadhrami, M. M. Ibrahim, Z. M. El-Bahy, C. Liu, C. Shen, and X. Liu, "Constructing nickel chain/MXene networks in melamine foam towards phase change materials for thermal energy management and absorption-dominated electromagnetic interference shielding," *Adv. Compos. Hybrid Mater.*, vol. 5, no. 2, pp. 755–765, Jun. 2022.

[31] W. Xie, F. Yao, H. Gu, A. Du, L. Qin, N. Naik, and Z. Guo, "Magnetoresistive and piezoresistive polyaniline nanoarrays in-situ polymerized surrounding magnetic graphene aerogel," *Adv. Compos. Hybrid Mater.*, vol. 5, no. 2, pp. 1003–1016, Jan. 2022.

[32] T. Gao, H. Rong, K. H. Mahmoud, J. Ruan, S. M. El-Bahy, A. A. Faheim, Y. Li, M. Huang, M. A. Nassan, and R. Zhao, "Iron/silicon carbide composites with tunable high-frequency magnetic and dielectric properties for potential electromagnetic wave absorption," *Adv. Compos. Hybrid Mater.*, vol. 5, no. 2, pp. 1158–1167, Jun. 2022.

[33] M. Quercio, E. Pošković, F. Franchini, E. Fracchia, L. Ferraris, A. Canova, A. Tenconi, H. Tiismus, and A. Kallaste, "Application of active thermography for the study of losses in components produced by laser powder bed fusion," *J. Magn. Magn. Mater.*, vol. 592, Jan. 2024, Art. no. 171796.

[34] M. Quercio, L. Barlassina, and A. Canova, "Characterization of the shielding properties of a power transformer enclosure," in *Proc. IEEE EUROCON 20th Int. Conf. Smart Technol.*, Jul. 2023, pp. 349–353.

[35] A. Kan, Q. Zhang, Z. Chen, and D. Cao, "Innovation on thermal conductivity measurement device of vacuum insulation panel with double hemispheres chambers," *ES Energy Environ.*, vol. 15, pp. 28–33, Jan. 2021.

[36] L. Santoro, R. Sesana, J. Diller, C. Radlbeck, and M. Mensinger, "Dissipative and thermal aspects in cyclic loading of additive manufactured AISI 316L," *Eng. Fail. Anal.*, vol. 163, May 2024, Art. no. 108446.

[37] E. D'Accardi, R. D. Finis, G. Dell'Avvocato, G. Masciopinto, D. Palumbo, and U. Galietti, "Conduction thermography for non-destructive assessment of fatigue cracks in metallic materials," *Infr. Phys. Technol.*, vol. 140, Jun. 2024, Art. no. 105394.

[38] E. D'Accardi, D. Palumbo, R. Tamborrino, and U. Galietti, "A quantitative comparison among different algorithms for defects detection on aluminum with the pulsed thermography technique," *Met.*, vol. 8, no. 10, p. 859, Oct. 2018.

[39] E. D'Accardi, A. Ulbricht, R. Krankenhagen, D. Palumbo, and U. Galietti, "Capability of active thermography to detect and localize pores in metal additive manufacturing materials," *IOP Conf. Series: Mater. Sci. Eng.*, vol. 1038, no. 1, Feb. 2021, Art. no. 012018.

[40] S. Doshvarpassand, C. Wu, and X. Wang, "An overview of corrosion defect characterization using active infrared thermography," *Infr. Phys. Technol.*, vol. 96, pp. 366–389, Jan. 2019.

[41] E. Thiel, M. Kreutzbruck, and M. Ziegler, "Laser projected photothermal thermography for characterizing hidden defects," in *Proc. 19th World Conf. Non-Destructive Test.*, 2016.

[42] A. Salazar, A. Mendioroz, and A. Oleaga, "Flying spot thermography: Quantitative assessment of thermal diffusivity and crack width," *J. Appl. Phys.*, vol. 127, no. 13, Apr. 2020, Art. no. 131101.

[43] L. Santoro, M. Quercio, A. Canova, and R. Sesana, "Measuring thermal and electrical performances of additively manufactured magnetic shielding material: An active thermography approach," *Nondestruct. Test. Eval.*, vol. 39, pp. 1–24, Jan. 2024, doi: 10.1080/10589759.2024.2305703.

[44] R. Sesana, L. Santoro, F. Curà, R. M. Nardo, and P. Pagano, "Assessing thermal properties of multipass weld beads using active thermography: Microstructural variations and anisotropy analysis," *Int. J. Adv. Manuf. Technol.*, vol. 128, nos. 5–6, pp. 2525–2536, Aug. 2023.

[45] L. Santoro, V. Razza, and M. D. Maddis, "Nugget and corona bond size measurement through active thermography and transfer learning model," *Int. J. Adv. Manuf. Technol.*, vol. 133, nos. 11–12, pp. 5883–5896, Jul. 2024, doi: 10.1007/s00170-024-14096-4.

[46] L. Santoro, V. Razza, and M. D. Maddis, "Frequency-based analysis of active laser thermography for spot weld quality assessment," *Int. J. Adv. Manuf. Technol.*, vol. 130, nos. 5–6, pp. 3017–3029, Dec. 2023, doi: 10.1007/s00170-023-12845-5.

[47] G. Dell'Avvocato, D. Gohlke, D. Palumbo, R. Krankenhagen, and U. Galietti, "Quantitative evaluation of the welded area in resistance projection welded (RPW) thin joints by pulsed laser thermography," *Proc. SPIE*, vol. 12109, pp. 152–165, may 2022.

[48] G. Dell'Avvocato and D. Palumbo, "Thermographic procedure for the assessment of resistance projection welds (RPW): Investigating parameters and mechanical performances," *J. Adv. Joining Processes*, vol. 9, Dec. 2023, Art. no. 100177.

[49] G. Dell'Avvocato, D. Palumbo, R. Pepe, and U. Galietti, "Non-destructive evaluation of resistance projection welded joints (RPW) by flash thermography," *IOP Conf. Ser., Mater. Sci. Eng.*, vol. 1038, no. 1, Feb. 2021, Art. no. 012003.

[50] C. Maierhofer, P. Myrach, R. Krankenhagen, M. Röllig, and H. Steinfurth, "Detection and characterization of defects in isotropic and anisotropic structures using lockin thermography," *J. Imag.*, vol. 1, no. 1, pp. 220–248, Dec. 2015.

[51] V. Borghese, L. Santoro, S. Santini, and R. Sesana, "Correlation between thermal and density properties of chestnuts: Preliminary results of experimental non-destructive testing," *Arch. Civil Mech. Eng.*, vol. 24, no. 3, pp. 1–15, May 2024, doi: 10.1007/s43452-024-00969-8.

[52] X. Guo and V. Vavilov, "Crack detection in aluminum parts by using ultrasound-excited infrared thermography," *Infr. Phys. Technol.*, vol. 61, pp. 149–156, Aug. 2013.

[53] H. Park, M. Choi, J. Park, and W. Kim, "A study on detection of micro-cracks in the dissimilar metal weld through ultrasound infrared thermography," *Infr. Phys. Technol.*, vol. 62, pp. 124–131, Nov. 2013.

[54] Q. Yi, H. Malekmohammadi, G. Y. Tian, S. Laureti, and M. Ricci, "Quantitative evaluation of crack depths on thin aluminum plate using eddy current pulse-compression thermography," *IEEE Trans. Ind. Informat.*, vol. 16, no. 6, pp. 3963–3973, Jun. 2020.

[55] B. Yuan, C. Spießberger, and T. I. Waag, "Eddy current thermography imaging for condition-based maintenance of overlay welded components under multi-degradation," *Mar. Struct.*, vol. 53, pp. 136–147, Feb. 2017.

[56] M. Goldammer, H. Mooshofer, M. Rothenfusser, J. Bass, J. Vrana, D. O. Thompson, and D. E. Chimenti, "Automated induction thermography of generator components," in *Proc. AIP Conf.*, vol. 1211, 2010, pp. 451–457.

[57] G. Dell'Avvocato, D. Palumbo, and U. Galietti, "A non-destructive thermographic procedure for the evaluation of heat treatment in Usibor® 1500 through the thermal diffusivity measurement," *NDT E Int.*, vol. 133, Jan. 2023, Art. no. 102748.

[58] H. Kato, T. Baba, and M. Okaji, "Anisotropic thermal-diffusivity measurements by a new laser-spot-heating technique," *Meas. Sci. Technol.*, vol. 12, no. 12, pp. 2074–2080, Nov. 2001.

[59] A. Wolf, P. Pohl, and R. Brendel, "Thermophysical analysis of thin films by lock-in thermography," *J. Appl. Phys.*, vol. 96, no. 11, pp. 6306–6312, Dec. 2004, doi: 10.1063/1.1811390.

[60] T. Ishizaki and H. Nagano, "Measurement of three-dimensional anisotropic thermal diffusivities for carbon fiber-reinforced plastics using lock-in thermography," *Int. J. Thermophys.*, vol. 36, nos. 10–11, pp. 2577–2589, Oct. 2014.

[61] K. Strzałkowski, M. Streza, D. Dadarlat, and A. Marasek, "Thermal characterization of II–VI binary crystals by photopyroelectric calorimetry and infrared lock-in thermography," *J. Thermal Anal. Calorimetry*, vol. 119, no. 1, pp. 319–327, Sep. 2014.

[62] A. Philipp, N. W. Pech-May, B. A. F. Kopera, A. M. Lechner, S. Rosenfeldt, and M. Retsch, "Direct measurement of the in-plane thermal diffusivity of semitransparent thin films by lock-in thermography: An extension of the slopes method," *Anal. Chem.*, vol. 91, no. 13, pp. 8476–8483, May 2019.

[63] D. Bavastro, A. Canova, L. Giaccone, and M. Manca, "Numerical and experimental development of multilayer magnetic shields," *Electric Power Syst. Res.*, vol. 116, pp. 374–380, Jul. 2014. [Online]. Available: https://www.sciencedirect.com/science/article/pii/S0378779614002375

[64] International Commission on Non-Ionizing Radiation Protection (ICNIRP), "Guidelines for limiting exposure to time-varying electric and magnetic fields (1 Hz to 100 kHz)," *Health Phys.*, vol. 99, no. 6, pp. 818–836, Dec. 2010.

[65] E. Salinas, O. Bottauscio, M. Chiampi, R. Conti, P. L. C. Romero, T. Dovan, P. Dular, J. Hoeffelman, R. Lindgren, P. Maioli, and G. Melik, "Mitigation techniques of power frequency magnetic fields originated from electric power systems," *Electra*, vol. 242, pp. 75–83, Jan. 2009.

[66] M. Quercio, F. Galbusera, A. Canova, A. G. Demir, G. Gruosso, and B. Previtali, "Electromagnetic shielding properties of LPBF produced Fe2.9wt.% Si alloy," *J. Phys., Energy*, vol. 5, no. 4, 2023, Art. no. 045003.

[67] A. Canova, F. Corti, A. Laudani, G. M. Lozito, and M. Quercio, "Innovative shielding technique for wireless power transfer systems," *IET Power Electron.*, vol. 17, no. 8, pp. 962–969, Sep. 2023.

[68] M. Quercio, F. Campanelli, and A. Canova, "Passive loop optimisation for HV joint zone," in *Proc. IEEE 20th Int. Conf. Smart Technol.*, Jul. 2023, pp. 343–348.

[69] A. Canova and M. Quercio, "A shielding system proposal for the cabling of electric glass melters," *IEEE Open J. Ind. Appl.*, vol. 4, pp. 1–10, 2023.

[70] J. Yu, Y. Zhang, Q. Guo, H. Hou, Y. Ma, and Y. Zhao, "Effect of pressure on anisotropy in elasticity, sound velocity, and thermal conductivity of vanadium borides," *Adv. Compos. Hybrid Mater.*, vol. 5, no. 3, pp. 2297–2305, Apr. 2022.

[71] D. Wei, M. Weng, M. H. H. Mahmoud, A. Y. Elnaggar, I. H. E. Azab, X. Sheng, M. Huang, Z. M. El-Bahy, and J. Huang, "Development of novel biomass hybrid aerogel supported composite phase change materials with improved light-thermal conversion and thermal energy storage capacity," *Adv. Compos. Hybrid Mater.*, vol. 5, no. 3, pp. 1910–1921, Jun. 2022.

[72] X. Jing, Y. Li, J. Zhu, C. Lei, S. Maganti, N. Naik, B. B. Xu, V. Murugadoss, M. Huang, and Z. Guo, "Improving thermal conductivity of polyethylene/polypropylene by styrene-ethylene-propylene-styrene wrapping hexagonal boron nitride at the phase interface," *Adv. Compos. Hybrid Mater.*, vol. 5, no. 2, pp. 1090–1099, Mar. 2022.

[73] L. Lu, X. Wang, S. Li, Y. Tang, and X. Mai, "Thermal performance of lonicera rupicola grass as a building insulation composite material," *Adv. Compos. Hybrid Mater.*, vol. 6, no. 1, p. 8, Dec. 2022.

[74] Z. Chang, K. Yuan, J. Li, Z. Sun, J. Zheng, M. Al-Fahdi, Y. Gao, B. Wei, X. Zhang, M. Hu, and D. Tang, "Anomalous thermal conductivity induced by high dispersive optical phonons in Rubidium and cesium halides," *ES Energy Environ.*, vol. 16, pp. 30–39, Jan. 2022.

[75] S. Verma, M. Dhangar, M. Mili, H. Bajpai, U. K. Dwivedi, N. Kumari, M. A. Khan, H. N. Bhargaw, S. A. R. Hashmi, and A. K. Srivastava, "Review on engineering designing of electromagnetic interference shielding materials using additive manufacturing," *Polym. Compos.*, vol. 43, no. 7, pp. 4081–4099, Apr. 2022, doi: 10.1002/pc.26684.

[76] K. Abedi, S. Miri, L. Gregorash, and K. Fayazbakhsh, "Evaluation of electromagnetic shielding properties of high-performance continuous carbon fiber composites fabricated by robotic 3D printing," *Additive Manuf.*, vol. 54, Mar. 2022, Art. no. 102733. [Online]. Available: https://www.sciencedirect.com/science/article/pii/S2214860422001373
[77] K. P. M. Lee, T. C. Baum, R. A. Shanks, and F. Daver, "Electromagnetic interference shielding of 3D-printed graphene–polyamide-6 composites with 3D-printed morphology," *Additive Manuf.*, vol. 43, May 2021, Art. no. 102020. [Online]. Available: https://www.sciencedirect.com/science/article/pii/S2214860421001858
[78] A. Mendioroz, R. Fuente, E. Apiñaniz, and A. Salazar, "Thermal diffusivity measurements of thin plates and filaments using lock-in thermography," *Rev. Sci. Instrum.*, vol. 80, no. 7, Jul. 2009, Art. no. 074904.
[79] H. Tiismus, A. Kallaste, T. Vaimann, and A. Rassõlkin, "State of the art of additively manufactured electromagnetic materials for topology optimized electrical machines," *Additive Manuf.*, vol. 55, Mar. 2022, Art. no. 102778. [Online]. Available: https://www.sciencedirect.com/science/article/pii/S2214860422001828
[80] H. Tiismus, A. Kallaste, T. Vaimann, L. F. Lind, I. Virro, A. Rassõlkin, and T. Dedova, "Laser additively manufactured magnetic core design and process for electrical machine applications," *Energies*, vol. 15, no. 10, p. 3665, May 2022. [Online]. Available: https://www.mdpi.com/1996-1073/15/10/3665
[81] H. Tiismus, A. Kallaste, A. Belahcen, A. Rassõlkin, and T. Vaimann, "Hysteresis loss evaluation of additively manufactured soft magnetic core," in *Proc. Int. Conf. Electr. Mach. (ICEM)*, vol. 1, Aug. 2020, pp. 1657–1661.
[82] S. Raab, R. Guschlbauer, M. A. Lodes, and C. Körner, "Thermal and electrical conductivity of 99.9% pure copper processed via selective electron beam melting," *Adv. Eng. Mater.*, vol. 18, no. 9, pp. 1661–1666, Jul. 2016, doi: 10.1002/adem.201600078.

MICHELE QUERCIO received the master's degree in mechanical engineering from Politecnico di Torino, in 2018, and the Ph.D. degree in electrical engineering, in 2022. He is currently a Researcher with the University of Roma Tre. His research interests include the computation of electromagnetic fields, design of magnetic shields, implementation of computational algorithms, renewable energy, and artificial intelligence. He is also actually convenor of the working group on non-destructive testing applied to the additive manufacturing sector of the European Federation for Non-Destructive Testing (EFNDT).

LUCA SANTORO is currently a dedicated Researcher with the Department of Mechanical and Aerospace Engineering, Politecnico di Torino. His expertise lies in non-destructive testing techniques and the mechanical fatigue of materials. He specializes in active thermography and innovative ultrasonic applications, with a recent focus on using thermography for monitoring welding processes. His work has led to significant industrial applications and the development of patents, contributing to advancements in material testing and engineering practices.

EMIR POSKOVIC (Member, IEEE) was born in Sarajevo, Bosnia and Herzegovina. He received the B.S. and M.Sc. degrees in electrical engineering from Polytechnic of Turin, in 2006 and 2008, respectively, and the Ph.D. degree in electrical energy engineering from the University of Padova, in 2020. He is currently an Assistant Professor with the Energy Department, Politecnico di Torino, and a Key Researcher for the Magnetic Characterization Laboratory, Alessandria Campus, Politecnico di Torino. He has published about 80 scientific papers in conference proceedings and technical journals. His special fields of interest included soft and hard magnetic materials, electrical machines, alternative, and renewable energy (micro-hydro, fuel cell, and PV-photovoltaic).

RAFFAELLA SESANA received the M.Sc. degree in mechanical engineering and the Ph.D. degree in machine design. She is currently an Associate Professor with the Department of Mechanic and Aerospace Engineering, Politecnico di Torino. Her main research interests include HCF, non-destructive fatigue limit and damage assessment, LCF and TMF damage models, characterization of materials and components, constitutive models for cyclic plastic behavior of metallic, polymeric materials, foams, and thermographic NDT.

ALDO CANOVA (Senior Member, IEEE) was born in Biella, Italy, in 1967. He received the Laurea and Ph.D. degrees in electrical engineering from Politecnico di Torino, Turin, Italy, in 1992 and 1996, respectively. In 1995, he became a Researcher, an Associate Professor, in 2003, and a Full Professor with the Energy Department "Galileo Ferraris," Politecnico di Torino, in 2017. He has authored/co-authored about 180 scientific publications in international conference proceedings and international journals and invented eight patents. He is involved in research activities related to the numerical computation of electromagnetic fields in the area of power devices and magnetic shielding, energy system modeling and optimization, and non-destructive testing. He has been a member of the Comitato Elettrotecnico Nazionale (CEI) serving on Technical Committee CT106 (methods for the assessment of electric, magnetic, and electromagnetic fields associated with human exposure), since 2004. He is also actually General Secretary of the Italian National Association of Non-Destructive Testing.

Open Access funding provided by 'Università degli Studi Roma Tre' within the CRUI CARE Agreement